Corrosion Science 114 (2017) 45–56

Contents lists available at ScienceDirect

Corrosion Science

journal homepage: www.elsevier.com/locate/corsci

Corrosion resistance and cytocompatibility of tantalum-surface-functionalized biomedical ZK60 Mg alloy

Weihong Jin [a], Guomin Wang [a], Zhengjie Lin [a,b], Hongqing Feng [a], Wan Li [a], Xiang Peng [a], Abdul Mateen Qasim [a], Paul K. Chu [a,*]

[a] Department of Physics and Materials Science, City University of Hong Kong, Tat Chee Avenue, Kowloon, Hong Kong, China
[b] Department of Orthopaedics & Traumatology, The University of Hong Kong, Pokfulam Road, Hong Kong, China

ARTICLE INFO

Article history:
Received 13 June 2016
Received in revised form 16 October 2016
Accepted 21 October 2016
Available online 22 October 2016

Keywords:
A. Mg
A. Sputtered films
A. Tantalum oxide
B. EIS
B. Polarization
B. SEM

ABSTRACT

Tantalum (Ta) is introduced to the surface of the ZK60 Mg alloy by reactive magnetron sputtering to enhance the corrosion resistance and cytocompatibility. The film thickness and composition, corrosion behavior, and cytocompatibility are studied by various techniques systematically. The surface layer composed of Ta_2O_5, Ta suboxide, and Ta increases the corrosion resistance of ZK60 while simultaneously improving cell attachment, spreading, and proliferation *in vitro*. The enhancement mechanism is proposed and discussed.

1. Introduction

As biodegradable materials, magnesium (Mg) and its alloys are promising in temporary implants including orthopedic implants [1,2] and cardiovascular stents [3,4]. Owing to natural degradation in the physiological environment, a follow-up surgery to remove the implant can be avoided after healing [5]. The biodegradable implant must provide sufficient mechanical support during tissue healing [6] but unfortunately, Mg-based biomedical implants tend to degrade too rapidly and sometimes even unpredictably under physiological conditions causing implant failure in severe cases [7]. In addition, rapid dissolution of Mg leads to other problems such as excessive hydrogen evolution, alkalinity, and detached degradation products [8,9]. Consequently, degradation of Mg-based alloys must be controlled while the biocompatibility must also be improved.

Development of suitable alloys and surface treatment are viable approaches to improve the properties of Mg alloys [10]. Mg alloys such as Mg–Ca, Mg–Sr, Mg–Zn, Mg–Si, Mg–Sn, and Mg–Zr show improved corrosion resistance and biosafety [9,11–13]. Compared to development of new Mg alloys, surface treatment is a simpler and more economical strategy to selectively tailor the surface corrosion resistance and biological properties [14–18]. In particular, reactive magnetron sputtering is a common technique to improve the corrosion resistance of different types of materials and industrial components [19–21]. It has been shown that tantalum (Ta) has good biocompatibility, osteogenesis, biosafety *in vivo* and there is no inflammatory response on Ta implants encapsulated with thin fibrous connective tissues [22]. Another study has shown that the bioactivity and biocompatibility of Ta stems from its ability to form a self-passivating surface oxide layer. From the perspective of orthopedic implants, this tantalum oxide (Ta_2O_5) layer can facilitate the formation of a bone-like apatite coating thus allowing bone and fibrous in-growth and rapid attachment of bone and soft tissues [23]. Moreover, Ta is one of the best anticorrosion metals due to the quick formation of an insulating Ta_2O_5 film in an aqueous medium [24–26]. The anticorrosion performance of Ta [27,28] and Ta_2O_5 [29–31] has been assessed. Lu et al. introduced Ta ions into polyetheretherketone by plasma immersion ion implantation to form Ta_2O_5 nanoparticles in the near surface which enhanced cell adhesion, proliferation of rat bone mesenchymal stem cells, and osteointegration *in vivo* [32]. Liu et al. deposited a nanocrystalline Ta coating on Ti-6Al–4V by reactive sputtering using a double glow discharge plasma technique and the β-Ta coating not only provided good corrosion protection, but also produced higher resistance against corrosion attack in Ringer's physiological solution at 37 °C than commercially pure Ta [33]. Xu et al.

* Corresponding author.
E-mail address: paul.chu@cityu.edu.hk (P.K. Chu).

http://dx.doi.org/10.1016/j.corsci.2016.10.021
0010-938X/

prepared a Ta_2O_5 nanoceramic coating by the double glow discharge plasma technique to enhance the corrosion resistance of biomedical Ti-6Al–4V. The Ta_2O_5 coating possessed excellent barrier properties against corrosion attack and provided long-term protection in simulated body fluids (SBF). Moreover, the potential of Ta_2O_5 as a corrosion resistant, biocompatible, as well as antibacterial coating on biomedical Ti and NiTi alloy has been investigated [34–37]. However, there have been few reports on the application of Ta_2O_5 to improve the corrosion resistance and biocompatibility of Mg-based alloys. In this paper, we present a novel surface modification concept and method to improve both the corrosion resistance and cytocompatibility of the ZK60 Mg alloy by introducing Ta into the alloy by reactive magnetron sputtering. Structural determination, electrochemical analysis, immersion tests, and biological experiments are performed systematically to evaluation the enhancement effects and pertinent mechanisms.

2. Experimental details

2.1. Sample preparation and surface characterization

The 10 mm × 10 mm × 4 mm specimens were prepared from the ZK60 (Mg – 5.04 wt% Zn – 0.52 wt% Zr) Mg alloy. Prior to deposition, the specimens were ground successively with 400–1200 grit SiC abrasive paper, ultrasonically rinsed in an ethanol bath for 15 min, and dried by nitrogen. The Ta_2O_5 films were deposited by direct-current reactive magnetron sputtering (ATC-Orion 5 UHV with Load-Lock, AJA International, Inc., Scituate, Massachusetts, USA) using argon as the sputtering gas, Ta as the sputtering target (99.99%), and nitrogen as the reactive gas. The base pressure was 6.5×10^{-4} Pa and working pressure was 0.50 Pa. The total flow rate during deposition was 12 sccm and the Ar/O_2 flux ratio was 1/1. The sputtering power was 100 W and deposition time was 3 h.

The cross sectional morphology and elemental maps were examined by scanning electron microscopy (SEM, JSM-820, JEOL Ltd., Tokyo, Japan) equipped with energy-dispersive X-ray spectroscopy (EDS, INCAx-sight, Oxford Instruments, Abingdon, Oxfordshire, UK). Grazing-incidence X-ray diffraction (GIXRD) was conducted on the SmartLab X-ray diffractometer (Rigaku Corporation, Tokyo, Japan) with Cu K_α radiation at an incident angle of 1° to determine the structure of the coatings. The XRD spectra were collected at angles between 15° and 80° at a rate of 0.02° s^{-1}. X-ray photoelectron spectroscopy (XPS, PHI 5802, Physical Electronics, Inc., Eden Prairie, Minnesota, USA) with Al K_α irradiation was conducted to determine the chemical states and the binding energies were referenced to the C 1s line at 284.8 eV.

2.2. Electrochemical studies and immersion tests

The electrochemical experiments were performed in SBF at 37 °C on an electrochemical workstation (Zennium, Zahner, Kansas City, Missouri, Germany) with the three-electrode configuration. The reference electrode was a saturated calomel electrode (SCE), the counter electrode was a platinum rod, and the sample served as the working electrode. All the potentials were referred to SCE if not specified. The SBF solution was prepared using reagent grade chemicals: 8.035 g/L NaCl, 0.355 g/L NaHCO3, 0.225 g/L KCl, 0.231 g/L $K_2HPO_4{\cdot}3H_2O$, 0.311 g/L $MgCl_2{\cdot}6H_2O$, 1.0 M HCl (39 mL), 0.292 g/L CaCl2, and 0.072 g/L Na_2SO_4 and deionized water. The SBF solution was buffered at pH 7.4 with 6.118 g/l trishydroxymethyl aminomethane and 1.0 M HCl. The ion concentrations in the SBF solution are 142.0 Na^+, 5.0 K^+, 1.5 Mg^{2+}, 2.5 Ca^{2+}, 147.8 Cl^-, 4.2 HCO_3^-, 1.0 HPO_4^-, and 0.5 SO_4^{2-} mM, which are close to those in human blood plasma [38]. The sample surface (1 cm^2) was exposed to the solution during the electrochemical measurements. Prior to electrochemical impedance spectroscopy (EIS), the samples were immersed in the solution for 5 min and EIS was then carried out at the open circuit potential (OCP) with a 10 mV alternating signal from 10 kHz to 100 mHz. Potentiodynamic polarization was performed on three independent samples at a scanning rate of 1 mV/s from −300 mV and 500 mV with respect to the OCP. To further investigate the corrosion characteristics of the untreated and coated ZK60 Mg alloy samples, they were immersed in 20 mL of SBF at 37 °C for 3 h, 24 h, and 48 h. The EIS and polarization data were not acquired during this stage. After rinsing with deionized water and drying with nitrogen, the surface and cross-sectional morphologies and composition were determined before and after immersion by SEM and EDS.

2.3. Direct cell adhesion and indirect cell proliferation

Mouse MC3T3-E1 pre-osteoblasts were used in the *in vitro* cell cultures. They were cultured in DMEM supplemented with 10% FBS at 37 °C in a humidified atmosphere with 5% CO_2. In the direct cell adhesion experiment, the specimens were sterilized with 70 vol% ethanol for 30 min and rinsed three times with sterile phosphate-buffered saline (PBS). 5×10^4 MC3T3-E1 cells per well were seeded ono the ZK60 and TO-ZK60 samples on a 24-well culture plate. After incubation for 8 h, the seeded samples were washed three times with sterile PBS followed by fixation with 4% paraformaldehyde for 15 min. Phalloidin fluorescein isothiocyanate (Sigma-Aldrich Corporation, St. Louis, Missouri, USA) was used to stain the cytoskeleton protein F-actin and 4′,6-diamidino-2-phenylindole (DAPI, Beyotime Institute of Biotechnology, Nantong, Jiangsu, China) was employed to stain the nuclei. Finally, the cells were observed under a fluorescence microscope (Axio Observer Z1, Carl Zeiss, Oberkochen, Germany). The morphology of the MC3T3-E1 preosteoblasts was also examined by SEM after incubation for 8 h. After culturing for 8 h, the cells were fixed by 4% paraformaldehyde for 15 min and after rinsing with PBS, the cells were dehydrated sequentially with a series of ethanol solutions (30%, 50%, 70%, 90%, and 100% for 10 min). The samples were sputter-coated with gold prior to SEM examination.

In the indirect cell proliferation evaluation, the extracts were prepared with DMEM in a humidified atmosphere with 5% CO_2 at 37 °C with a surface area/extracts ratio of 1 cm^2/mL. After 72 h, the extracts were collected, filtered through a 0.22 um filter (Merck Millipore, Billerica, Massachusetts, USA), and refrigerated at 4 °C prior to the cell proliferation experiments. To monitor the change in the extracts compared to the fresh DMEM, the concentrations of leached Mg, alloying elements, calcium (Ca), and phosphorus (P) were determined by inductively-coupled plasma optical emission spectroscopy (ICP-OES, PE Optima 2100DV, Perkin Elmer, Waltham, Massachusetts, USA). The pH of the collected extracts was also monitored.

The MC3T3-E1 cells were seeded at a density of 5.0×10^3 per well on a 96-well culture plate for 24 h 100 μL of the extracts supplemented with 10% FBS were used to replace the previous medium. The control group was treated with DMEM supplemented with 10% FBS. After incubation for 1, 3, and 6 days, 10 μL of (3-(4,5-dimethylthiazol-2-yl)-2,5-diphe-nyltetrazolium bromide at a concentration of 5 μg/mL were added to each well and 100 μL of dimethyl sulfoxide were added to dissolve the formed formazen after incubation for 4 h. The absorbance at 570 nm was monitored on a microplate spectrophotometer (BioTek Eon, BioTek Instruments Inc., Winooski, Vermont, USA). The background absorption at 690 nm was subtracted and the cell viability was calculated by the following relationship: $(OD_{sample}/OD_{control}) \times 100\%$.

After incubation for 1 and 3 days, cell proliferation was also assessed using the Cell Proliferation ELISA, BrdU kit (Roche Applied Science, Penzberg, Upper Bavaria, Germany). The cells were first

labeled with the BrdU labeling medium at 37 °C for 4 h. The cells were fixed for 30 min at room temperature and incubated with the anti-BrdU-POD working solution for 2 h. After rinsing several times with PBS, the solution was applied to each well. Finally, the reaction was stopped by 1 M H_2SO_4 and the absorbance was monitored at 450 nm on the microplate spectrophotometer (BioTek Eon, BioTek Instruments Inc., Winooski, Vermont, USA).

3. Results and discussion

3.1. Surface characterization

Fig. 1(a) and (b) present the XPS full spectrum and high-resolution Ta 4f spectrum of TO-ZK60. As shown in Fig. 1(a), only Ta and O are detected. The high-resolution XPS Ta 4f spectrum (Fig. 1(b)) can be deconvoluted into several peaks. With regard to the Ta states, the spin-orbit doublet separation is 1.9 eV and the intensity ratio between Ta $4f_{7/2}$ and Ta $4f_{5/2}$ peak is 4/3. The Ta 4f spectrum is separated into four sets of $4f_{7/2}$ and $4f_{5/2}$ peaks of the oxidized and metallic states. The peaks at 26.0 eV for Ta $4f_{7/2}$ and 27.9 eV for Ta $4f_{5/2}$ are assigned to a typical chemical state of Ta in Ta_2O_5 [39–41]. The Ta 4f spectrum also shows two peaks at binding energies of 21.5 eV and 23.4 eV corresponding to metallic Ta [40,42,43]. The existence of Ta suboxide in the film is confirmed by the two sets of peaks between the Ta^{5+} and metallic Ta [44,45]. Hence, reactive magnetron sputtering produces a surface layer composed of Ta_2O_5, Ta suboxide, and Ta (TO) on the ZK60 Mg alloy. The crystallinity of the films is assessed by the GLXRD spectrum of the TO-coated silicon in Fig. 1(c). Since broad diffraction peaks appear at approximately 20°–40° and 42°–66°, the films have an amorphous structure which is in agreement with data in the literature [34,46–48]. The cross-sectional SEM image of the TO-coated ZK60 (TO-ZK60) sample in Fig. 1(d) shows a thickness of 1.48 ± 0.02 μm. The films are quite homogeneous and dense and no obvious micro-defects and pinholes are observed. Meanwhile, the films adhere tightly to the substrate. The results reveal that amorphous, homogeneous, compact, and adherent films composed of Ta_2O_5, Ta suboxide, and metallic Ta films are prepared on the ZK60 substrate by reactive sputtering.

3.2. Corrosion behavior

Prior to the EIS and polarization tests, the OCP of the untreated ZK60 and TO-ZK60 are monitored for 300 s after immersion in SBF as shown in Fig. 2(a). The OCP of the untreated and treated ZK60 samples increases slightly with immersion time in SBF. After immersion in SBF for 300 s, the potential of the untreated ZK60 changes from −1754 to −1707 mV vs. SCE, whereas that of TO-ZK60 shifts from −1709 to −1665 mV vs. SCE. After immersion for 5 min, the untreated ZK60 and TO-ZK60 show potential shifts of 47 and 44 mV vs. SCE. The materials may be in the steady state sufficiently to measure the impedance after 5 min immersion. According to the observed trend, the OCP of the untreated and treated ZK60 may make a further positive shift and the potential shift of TO-ZK60 is likely to be smaller than that of ZK60 after a longer time. We will conduct more experiments in the future to confirm this.

The polarization curves acquired from ZK60 and TO-ZK60 in SBF are displayed in Fig. 2(b). The anodic and cathodic polarization curves represent dissolution of the samples and hydrogen evolution, respectively. Since the anodic and cathodic branches are asymmetrical [49], the corrosion potential (E_{corr}) and corrosion current density (I_{corr}) are determined by Tafel extrapolation of the cathodic polarization curve. The E_{corr}, I_{corr}, and Tafel slope β_c values obtained from the polarization curves are listed in Table 1. The E_{corr} value of the untreated ZK60 is −1672 mV vs. SCE in SBF, whereas that of the TO-ZK60 Mg alloy shows a positive shift to −1565 mV vs. SCE in SBF, suggesting that corrosion of ZK60 in SBF is retarded by the Ta-containing film. The TO-ZK60 sample exhibits smaller I_{corr} of 1.334 ± 0.066 μA/cm² in SBF than ZK60 (724.0 ± 86.1 μA/cm² in SBF), indicating an approximate 543-fold decrease in I_{corr} compared to the untreated substrate in SBF. The smaller the corrosion current density, the lower is the corrosion rate. Jamesh et al. [50] modified the ZK60 Mg alloy by Zr, O, Zr&O implantation and the smallest I_{corr} of 11 μA/cm² was observed from the Zr&O co-implanted ZK60 in SBF. Xu et al. [51] conducted carbon ion implantation into pure Mg and obtained an I_{corr} value of 26.3 μA/cm² in SBF. Li et al. [52] obtained an I_{corr} value of 11.9 μA/cm² in SBF from dicalcium phosphatedihydrate/poly(lactic-co-glycolic acid) hybrid coated-AZ31 Mg alloy fabricated by electrochemical deposition. Zhou et al. [53] explored ways to improve the corrosion behavior of AZ91D magnesium alloy by conducting heat treatment and I_{corr} of the heat-treated samples in SBF decreased to 27 μA/cm². Herein, modification of the ZK60 Mg alloy results in a decrease of I_{corr} to 1.334 ± 0.066 μA/cm² in SBF, which is much smaller than those observed from modified ZK60 and other Mg alloys reported in the literature. The polarization results reveal that degradation of the ZK60 Mg alloy is greatly retarded by the Ta-containing film.

Table 1
E_{corr}, I_{corr}, and β_c of ZK60 and TO-ZK60 in SBF calculated from the polarization curves.

	E_{corr} (mV vs. SCE)	I_{corr} (μA/cm²)	β_c (mV/decade)
ZK60	−1672 ± 6	724.0 ± 86.1	−360 ± 6
TO-ZK60	−1565 ± 19	1.334 ± 0.066	−574 ± 22

Data are shown as mean ± standard deviation (n=3).

EIS is performed to obtain insights into the corrosion processes of the untreated and coated ZK60 Mg samples and both the Nyquist and Bode plots of the ZK60 and TO-ZK60 samples in SBF are shown in Fig. 2(c)–(e). The Nyquist plots of ZK60 and TO-ZK60 exhibit three semi-circles corresponding to three time constants. The TO-ZK60 sample shows larger capacitive loops at high and medium/low frequencies suggesting improved corrosion resistance. An electrical equivalent circuit with three time constants shown in Fig. 2(f) is used to fit the experimental EIS data with an inductive arc. R_s corresponds to the solution resistance between the reference electrode and sample, CPE_1 is the capacitance of the deposited film or corrosion products, and R_1 is the corresponding resistance, which is closely related to the coating thickness and defects especially the amount of pores [54]. CPE_2 represents the double layer capacitance at the electrolyte/substrate surface and R_2 represents the relevant charge transfer resistance. A similar equivalent circuit has been used to explain the corrosion behavior of ZK60 Mg alloy [50], Mg-Ca, and Mg-Sr [55] as well as untreated and coated AZ91D in m-SBF after surface modification [56]. The electrical equivalent circuits reveal good fits in the Nyquist and Bode plots and the fitted results are listed in Table 2. In SBF, the TO-ZK60 sample shows a large increase in R_1 (from 59.46 Ω cm² to 2.313×10^4 Ω cm²) and R_2 (12.57 Ω cm² to 2.870×10^4 Ω cm²) along with smaller CPE_1 and CPE_2. This means that corrosion of the TO-ZK60 sample is mitigated in SBF. The untreated ZK60 has smaller R_1 and R_2 due to the loose and porous corrosion layer on the surface, which is not able to protect the substrate against the corrosive medium as effectively. The obviously larger R_1 and R_2 of the coated ZK60 sample are attributed to the surface layer containing Ta_2O_5, Ta suboxide, and Ta. According to recent studies, carbon ion implantation into pure Mg increased the film resistance and charge transfer resistance in SBF to 19.23 and 737.4 Ω cm², respectively [51]. The film resistance and charge transfer resistance of the as-cast WE43 Mg alloy modified by Zr&N implantation in SBF increased to 737.0 and 828.7 Ω cm², respectively [57]. The dicalcium phosphatedihydrate/poly(lactic-

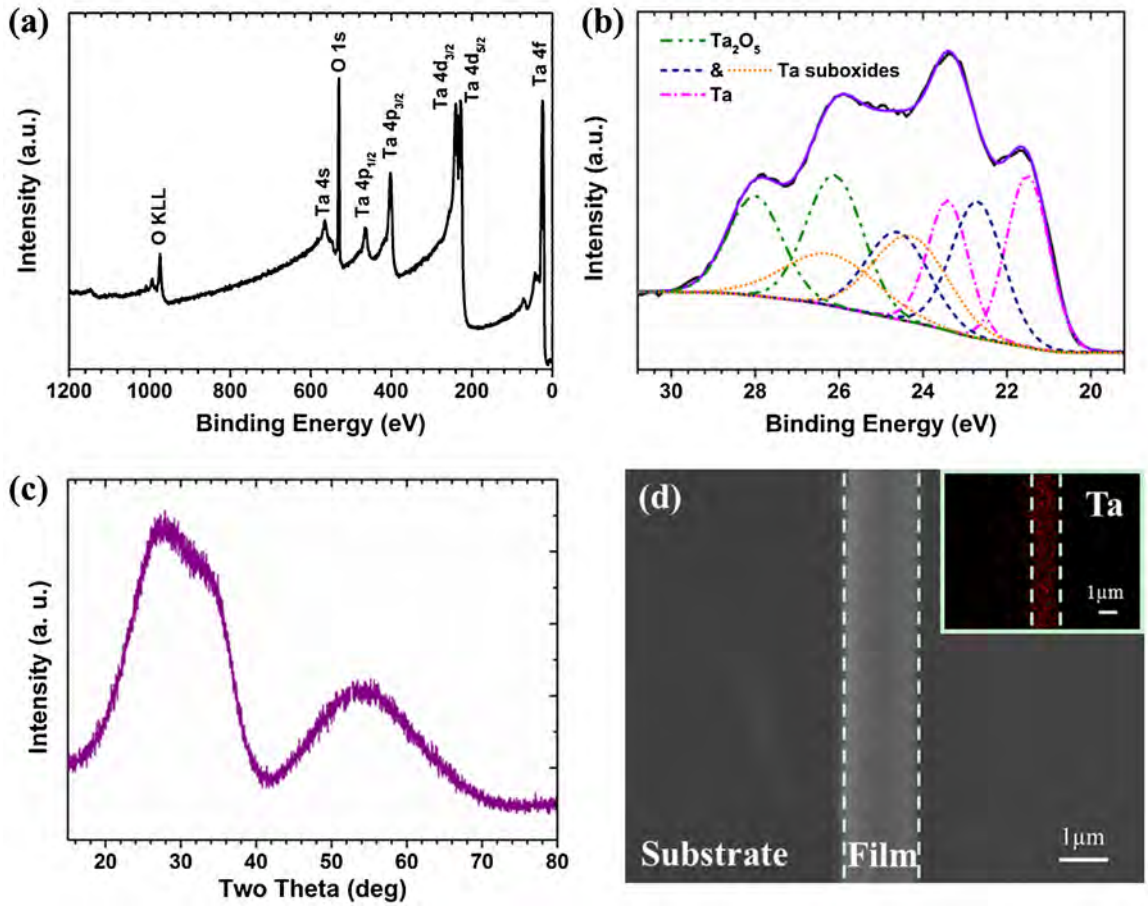

Fig. 1. (a) XPS full spectrum of TO-ZK60 and high-resolution XPS spectra of (b) Ta 4f acquired from TO-ZK60 after sputtering for 50 nm. (c) Cross-section of the TO film on ZK60 examined by SEM. (d) GLXRD spectrum of the TO-coated silicon.

Table 2
Fitted EIS results of ZK60 and TO-ZK60 in SBF based on the corresponding equivalent circuit models.

	R_s (Ω cm^2)	CPE_1 (Ω^{-1} cm^{-2} s^{-n})	n_1	R_1 (Ω cm^2)	CPE_2 (Ω^{-1} cm^{-2} s^{-n})	n_2	R_2 (Ω cm^2)
ZK60	20.81	3.103×10^{-5}	0.86	59.46	4.949×10^{-3}	1	12.57
TO-ZK60	19.49	1.933×10^{-7}	0.80	2.313×10^{4}	6.253×10^{-6}	0.77	2.87×10^{4}

co-glycolic acid) coated-AZ31 Mg alloy showed film resistance and charge transfer resistance of 84.3 and 3190 Ω cm^2 in SBF [52]. The results show that the corrosion resistance of the Ta-incorporated ZK60 is enhanced.

The Bode impedance and phase angle plots of the ZK60 and TO-ZK60 samples acquired in SBF in Fig. 2(d) and (e) provide anti-corrosion information from different perspectives. TO-ZK60 shows larger impedance and phase angle over a large range of frequencies compared to the untreated substrate. The impedance of the coated ZK60 alloy at the low frequency of 100 mHz rises from 84.7 Ω cm^2 (untreated ZK60) to 4.052×10^4 Ω cm^2 in SBF indicative of dramatically enhanced resistance against the corrosive media [58]. The maximum phase angle of ZK60 is 29.4°, whereas that of TO-ZK60 increases to 65.2° in SBF. The larger phase angle corresponds to the more capacitive response, suggesting that the Ta-functionalized surface provides good protection for the metallic ZK60 substrate under the corrosive conditions [59]. The Bode impedance and phase angle results agree with those obtained by the Nyquist plots.

Before and after the immersion tests, the surface morphology of the ZK60 and TO-ZK60 samples was observed by SEM. As shown in Fig. 3(a) and (b), both the untreated and coated ZK60 samples have a relatively rough surface with some scratches produced by mechanical grinding during specimen preparation. The film surface is further observed at high magnification. Fig. 3(c) shows that the ZK60 surface is covered by a dense and continuous film with small grains. However, some defects such as cracks and large particles indicated by arrows in Fig. 3(d) are observed from the film and they may be due to incomplete removal of contaminants from the substrate surface during sample preparation or low substrate temperature during film deposition. Fig. 4 depicts the SEM images at different magnifications after immersion in SBF for 3, 24, and 48 h. According to the surface morphological images, corrosion spreads rapidly across the entire surface of the untreated ZK60 during immersion. At each time point, the untreated ZK60 samples exhibits more severe corrosion. After immersion for 48 h in SBF, the untreated ZK60 shows a completely corroded surface with cracks that are relatively long and wide (referred to by an arrow). These cracks act as channels for penetration of the corrosive solution leading to further dissolution of the metallic substrate. Fig. 4(c) shows that after immersion for 48 h, the corrosion layer consists of outer and inner layers as indicated by the red circle. Similar results have been obtained from corroded ZK60 and pure Mg soaked in SBF [60,61]. The fresh Mg substrate suffers from further attack and corrosion due to penetration of the corrosive medium through the

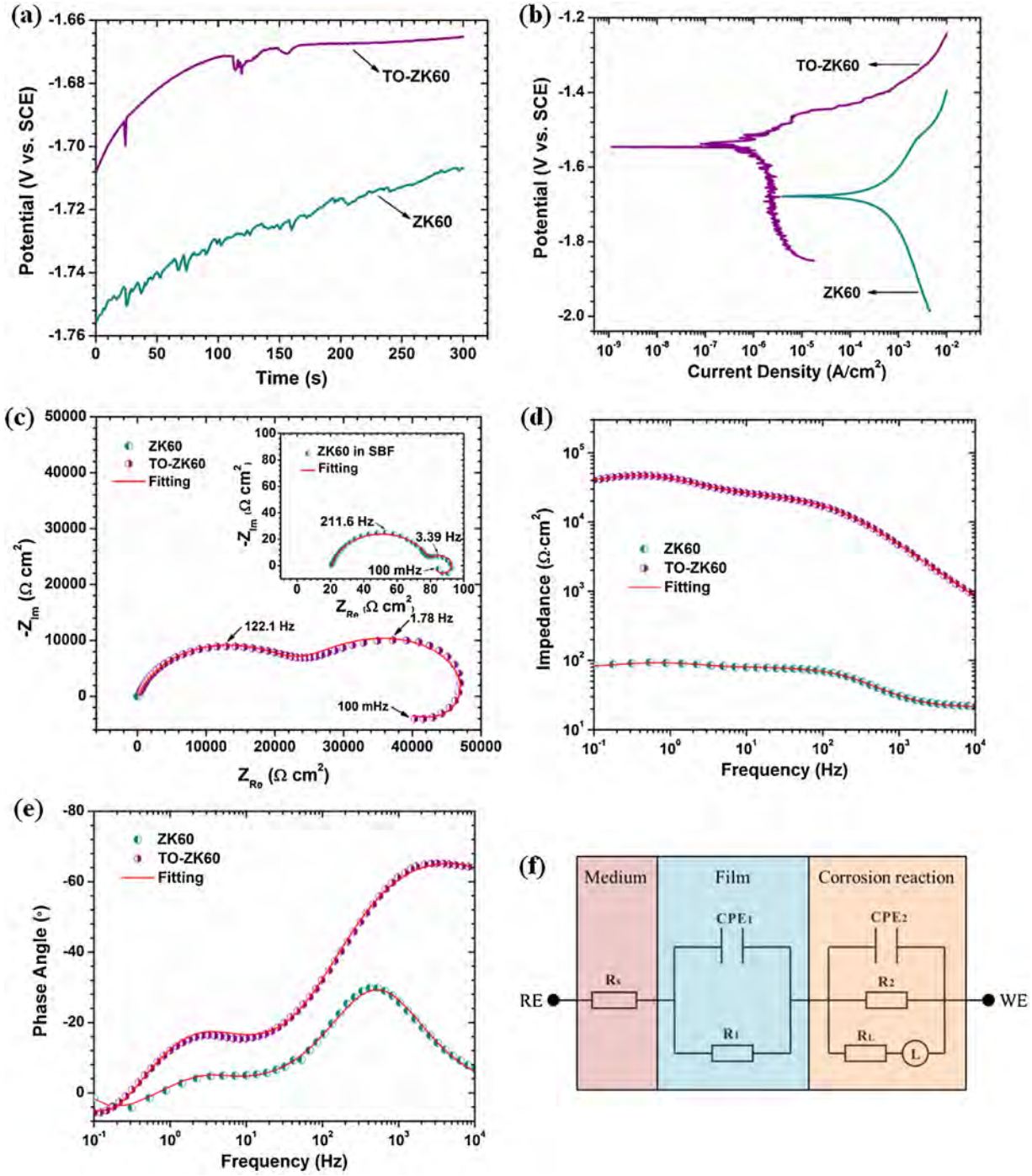

Fig. 2. (a) OCP of ZK60 and TO-ZK60 in SBF for 300 s. (b) Polarization curves following (c) Nyquist plots, (d) Bode impedance and (e) phase angle plots monitored after 5 min immersion, and (f) corresponding equivalent circuits of ZK60 and TO-ZK60 in SBF.

outer porous corrosion layer. Compared to the severe corrosion on the untreated ZK60 sample, corrosion initiation is delayed significantly and also slower after surface treatment. No corrosion occurs on the TO-ZK60 surface after immersion for 3 and 24 h SBF. As shown in Fig. 4(f), when the immersion time is extended to 48 h, the TO-ZK60 sample does show some local corrosion which is caused by corrosive solution penetration through the defects in the film and subsequently onto the Mg alloy substrate leading to the dissolution. However, the extent of corrosion on TO-ZK60 is much less than that on the untreated ZK60. In fact, most of the regions on the TO-ZK60 sample surface are fresh and intact. The area of the corroded region on TO-ZK60 is much less and the surface cracks are fewer, shorter, and narrower.

To further investigate corrosion propagation along the depth as well as elemental distribution in the cross sections, SEM images and EDS maps are acquired from ZK60 and TO-ZK60. As shown in Figs. 5 and 6, two red dash lines are used to label the original sample surface before the immersion test (right) and the maximum depth of corrosion after the immersion test (left), respectively. Fig. 5(a) shows that the maximum thicknesses (the distance between the two red dash lines) of the corrosion products on the untreated ZK60 are 21.4, 48.9, and 180.4 μm after immersion for 3, 24, and 48 h in SBF, respectively. On the other hand, Fig. 6(a) does not reveal a cor-

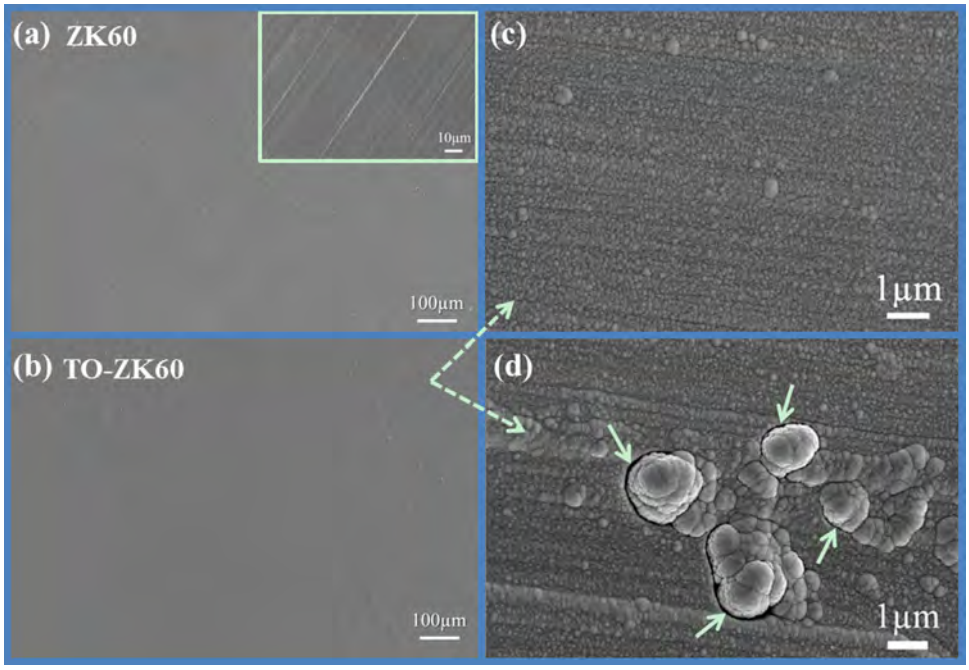

Fig. 3. Surface morphology of the (a) ZK60 and (b, c, d) TO-ZK60 samples at different magnifications before immersion in SBF.

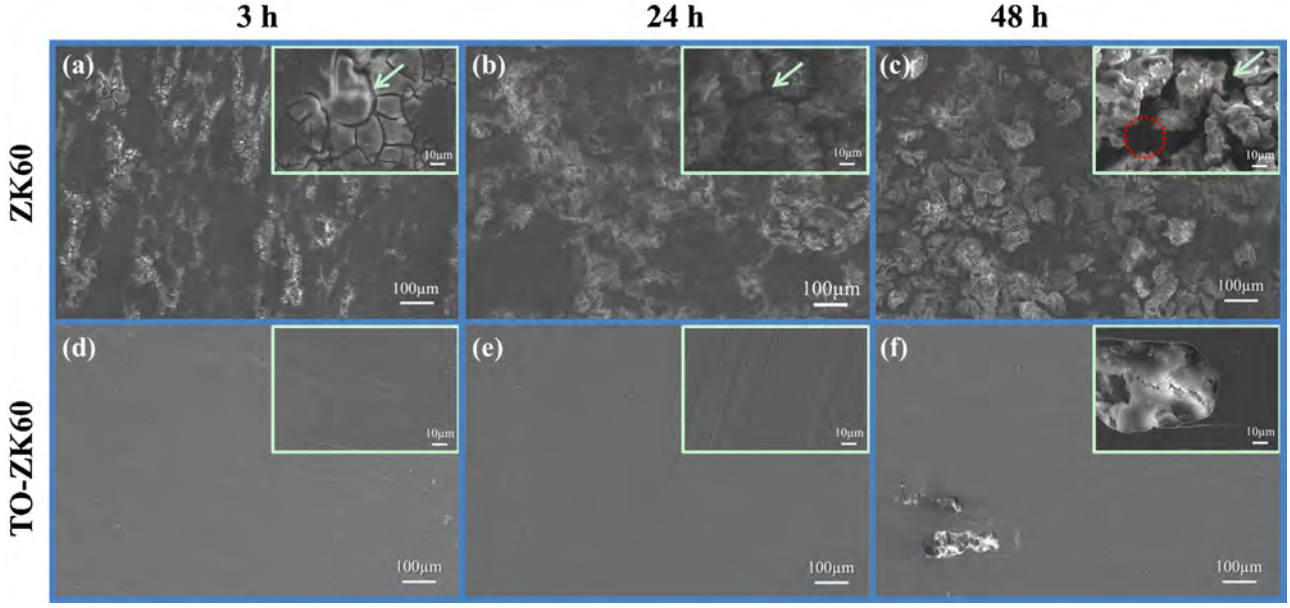

Fig. 4. Surface morphology of the (a, b, c) ZK60 and (d, e, f) TO-ZK60 samples after immersionin SBF for 3 h, 24 h, and 48 h.

rosion layer on the treated ZK60 sample after immersion for 24 h. Even when the immersion time is increased to 48 h, the corrosion layer on TO-ZK60 is only 21.3 μm thick. The thickness of corrosion products on the untreated ZK60 is 8.5 times that on the treated ZK60 sample after 48 h indicating that TO-ZK60 experiences less corrosion and corrosion propagation in SBF. It is noted that the corrosion layer comprises an outer layer (labeled by the blue rectangle) and inner layer. A portion of the corrosion layer is filled with resin which may lead to padding of the holes or delamination of the outer corrosion layer

Figs. 5 (b) and (c) and 6 (b) and (c) present the EDS maps of the cross sections of ZK60 and TO-ZK60 after immersion in SBF. Mg, P, Ca, and Zn except O are observed (the background of O as a light element is high) [57,62]. The corrosion products on the untreated ZK60 samples are composed of Mg, P, Ca, as well as O, which may be assigned to the formation of MgO, $Mg(OH)_2$, phosphate, and carbonate during immersion [63]. With regard to ZK60, the Mg signal from the corrosion product layers is smaller than that from the substrate since Mg dissolves to form corrosion products together with other elements in the immersion solution. Zn is detected from the substrate and corrosion layers but the intensity is quite small. Hence, the Mg signal can be directly used to differentiate the corrosion regions from the fresh substrate and the results are in agreement with the SEM images obtained from the cross-sections. The intensity of the detected elements, especially P and Ca, varies with immersion time. After short immersion for 3 h, the P and Ca signals from ZK60 are weak because the sample experiences less severe corrosion and the signals are strong after immersion for

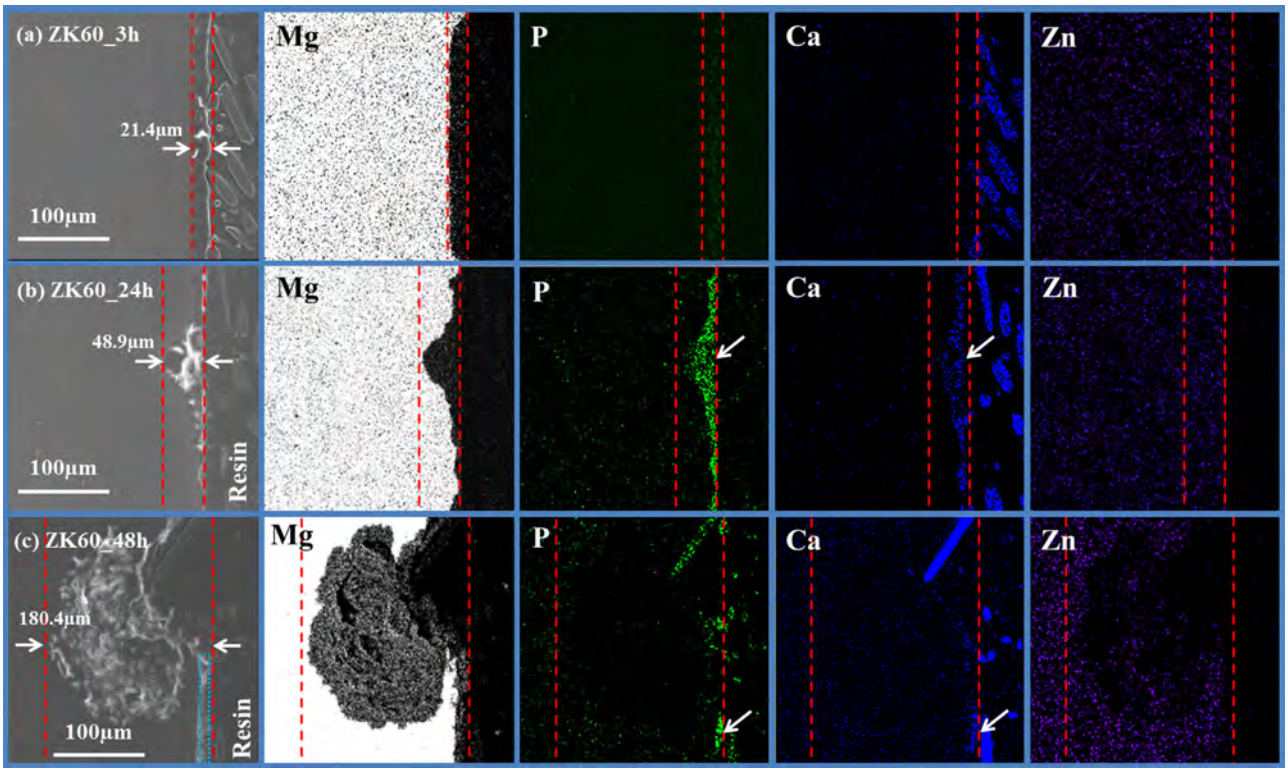

Fig. 5. SEM cross-sectional images and corresponding EDS maps of ZK60 after immersion in SBF for (a) 3 h, (b) 24 h, and (c) 48 h. (For interpretation of the references to color in the text, the reader is referred to the web version of this article.)

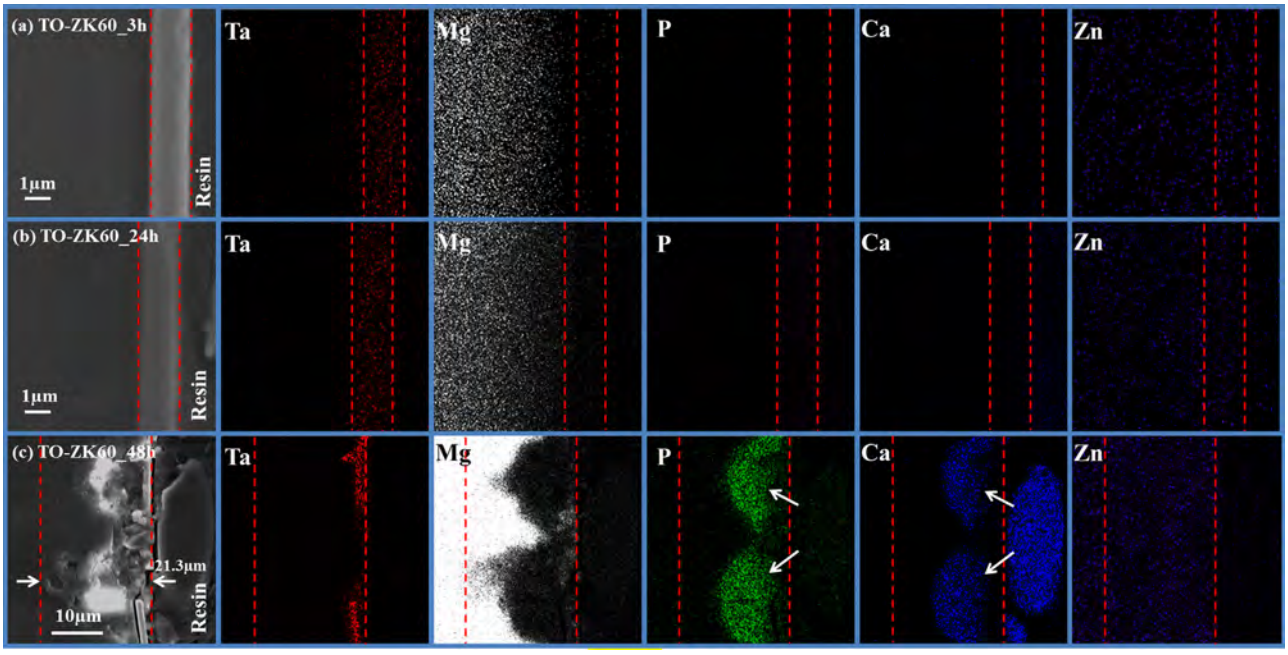

Fig. 6. SEM cross-sectional images and corresponding EDS maps of TO-ZK60 after immersion in SBF for (a) 3 h, (b) 24 h, and (c) 48 h. (For interpretation of the references to color in the text, the reader is referred to the web version of this article.)

24 h. If ZK60 sample is immersed in SBF for 48 h, obvious P and Ca signals are observed from the outer corrosion layer (referring to the arrows). These results suggest that corrosion on ZK60 proceeds gradually in SBF with time and the P and Ca contents in the corrosion product layers increase until the metallic Mg substrate is totally consumed. When the immersion time is prolonged to 48 h, stronger P and Ca signals are detected from the outer layer than the inner one providing evidence that the P and Ca contents increase with the degree of corrosion.

The Ta-containing film on TO-ZK60 maintains its integrity and no P and Ca are detected after soaking in SBF solution for 3 h and 24 h because no corrosion layer is formed. Breakage is observed from the Ta-containing film deposited on ZK60 after immersion for 48 h. The maximum thickness of the corrosion product layer on

the corroded region of TO-ZK60 is 21.3 μm, which is much smaller than that on ZK60. The corrosion products are composed of Mg, P, and Ca. TO-ZK60 shows less corrosion propagation due to the surface layer comprising Ta_2O_5, Ta suboxide, and Ta. It is difficult for the corrosive solution to penetrate a homogeneous, dense, and adhesive film and so the film here isolates the Mg substrate from the corrosive solution, retards substrate degradation, and enhances the corrosion resistance of the ZK60 Mg alloy.

With regard to the untreated ZK60 Mg alloy immersed in the corrosive solution, the solution penetrates the thin and porous native $MgO/Mg(OH)_2$ layer into the Mg substrate. The metallic Mg with a standard potential of −2.37 V dissolves to form Mg^{2+} upon contact with the corrosive solution (Eq. (1)). In this process, hydrogen is formed and the local alkalinity increases (Eq. (2)). The insoluble Mg hydroxide is formed in the local corroded regions (Eq. (3)).

$$Mg(s) \rightarrow Mg^{2+}(aq) + 2e^{-}(\text{anodicreaction}) \quad (1)$$

$$H_2O(aq) + 2e^{-} \rightarrow H_2(g) + 2OH^{-}(aq)(\text{cathodicreaction}) \quad (2)$$

$$Mg^{2+}(aq) + 2OH^{-}(aq) \rightarrow Mg(OH)_2(s)(\text{productformation}) \quad (3)$$

The corrosion products formed on the substrate serve as barriers against further corrosion. However, very limited protection is rendered by this layer because $Mg(OH)_2$ has a loose structure as confirmed by the SEM images. The cracks in the corrosion product layer serve as channels between the external solution and metallic substrate. The insoluble $Mg(OH)_2$ tends to be transformed into soluble $MgCl_2$ when exposed to a medium containing Cl^- to further weaken the protection. Therefore, the Mg substrate is easily and continuously consumed by the corrosive medium and a high dissolution rate results. The electrochemical studies indicate that the untreated ZK60 Mg alloy has small R_1 and R_2 implying low resistance against mass transportation through the corrosion layer and charge transfer at the oxide layer/substrate interface due to the loose corrosion layer which only offers partial protection. After immersion for 48 h in SBF, the whole surface of the ZK60 sample is covered by the corrosion layer as a result of lateral spreading of Mg dissolution and dissolution and delamination of the outer layer. Rapid corrosion penetration along the depth direction of ZK60 is verified by the cross-sectional SEM images. Accompanying the corrosion process, Mg phosphate and carbonate are gradually formed on the base of $Mg(OH)_2$. EDS analysis of the corrosion products confirms that Mg, P, and Ca are the major elements in the corrosion products. The cross-sectional EDS data show that the concentrations of P and Ca in the outer corrosion product layer are larger than those in the inner layer close to the substrate. This implies that corrosion marches gradually into the substrate. The untreated ZK60 Mg alloy shows a large I_{corr} which is directly proportional to the corrosion rate. Hence, corrosion of the ZK60 Mg alloy is caused by the high intrinsic Mg dissolution which is not mitigated significantly by the loose corrosion products on the ZK60 surface.

A surface layer containing inert Ta_2O_5, Ta suboxide, and Ta is formed by reactive magnetron sputtering on TO-ZK60. Although the layer covers the substrate uniformly, the corrosive species can still reach the metallic substrate through a few weak spots inducing local corrosion. However, it is more difficult for the corrosion species to penetrate the tantalum oxide film barrier to corrode the Mg substrate. The SEM images of the surface and cross section of the immersed TO-ZK60 sample provide evidence that only the film in a small region breaks down after immersion for 48 h in SBF and the corrosion layer is much thinner than that on the untreated one. Both vertical and lateral spreading of Mg consumption in SBF is retarded by the surface layer which increases the mass transportation resistance R_1 and charge transfer resistance R_2 leading to reduced corrosive medium access to the metallic substrate and decreased galvanic corrosion. The small I_{corr} values calculated from polarization curves of the modified ZK60 are also in accordance with the EIS and immersion results.

3.3. in vitro *cell adhesion and cell proliferation*

Biomedical implants must have not only good mechanical properties and corrosion resistance, but also suitable biological characteristics. Fig. 7 displays the direct response of MC3T3-E1 pre-osteoblasts on the untreated and coated ZK60 Mg samples. After immersion for 8 h, a few cells are observed from the untreated substrate but there are more attached cells on the modified sample as shown in Fig. 7(a)–(d). In fact, the MC3T3-E1 cells on the untreated ZK60 suffer from morphological damage becoming rounder with a smaller cellular diameter, whereas the cells on the coated sample exhibit an elongated shape, good spreading, as well as more actin filaments and actin stress fibers (Fig. 7(a)–(f)). The average cell number and surface area increase from 14 to 122 and from 1957.9 μm^2 to 20939.9 μm^2 (Fig. 7(g)) after surface treatment, showing that the untreated ZK60 Mg alloy does not support initial cell attachment and spreading. The improved initial cellular characteristics observed from TO-ZK60 are prerequisite to ensuing cell growth and proliferation.

The *in vitro* cell cytotoxicity of ZK60 before and after surface treatment and after 1, 3, and 6 days is presented in Fig. 8(a). At each time point, 70% extract of the untreated ZK60 exhibits high cell cytotoxicity to the MC3T3-E1 cells due to the obviously reduced cell viability of the MC3T3-E1 pre-osteoblasts cultured in the ZK60 extracts. When the cells are incubated with the ZK60 extracts for 6 days, few live cells remain. The viable cell number incubated with the TO-ZK60 extracts is larger than that incubated with the untreated ZK60 extracts. The cell viability of the MC3T3-E1 pre-osteoblasts retains a high level of 83% after culturing with the TO-ZK60 extracts for 6 days implying slight cytotoxicity of TO-ZK60 Mg and good cell proliferation during incubation with the TO-ZK60 extracts. Fig. 8(b) shows the fold change of BrdU incorporation after 1 and 3 days. When the 50% extract is used, obviously increased BrdU incorporation is observed from the TO-ZK60 samples throughout the culturing period compared to the untreated group, suggesting that the MC3T3-E1 cells in the S phase and cell proliferation rate are enhanced by the Ta-containing film. These *in vitro* results reveal improved cell proliferation after the surface and more robust bone–implant bonding is expected *in vivo* as higher osteoblast proliferation leads to a larger mass of bone tissues around the implant.

The corrosion of Mg alloy can affect the direct and indirect cellular behavior. The interface condition is greatly changed if corrosion of the Mg alloy is too rapid subsequently leading to an alkaline environment, released metal ions, and hydrogen bubbles. As mentioned above, the TO-ZK60 Mg alloy has excellent corrosion resistance in SBF. The enhanced corrosion resistance mitigates these changes in the interface providing a relatively stable surface to allow better cell attachment and cell spreading which can be achieved in a friendly environment with less adverse stimulation. Meanwhile, according to previous studies, Ta and Ta_2O_5 have excellent biocompatibility [22,23]. This biocompatible and corrosion resistant TO film maintains a relatively biocompatible and stable surface allowing the cells to adhere and spread on the surface.

The indirect cell proliferation may be affected by ions released from the Mg alloy into DMEM during preparation of the extracts as well as increased pH of the prepared extracts. As shown in Fig. 9(a), the untreated ZK60 extracts show a significant decrease in the P and Ca concentrations attributable to the formation of insoluble P and Ca precipitates on the substrate in concert with rapid degradation of the ZK60 Mg alloy. Since the corrosion products have a loose and porous structure, they may delaminate in the cell culture medium producing adverse effects to the cultured cells. Even though the

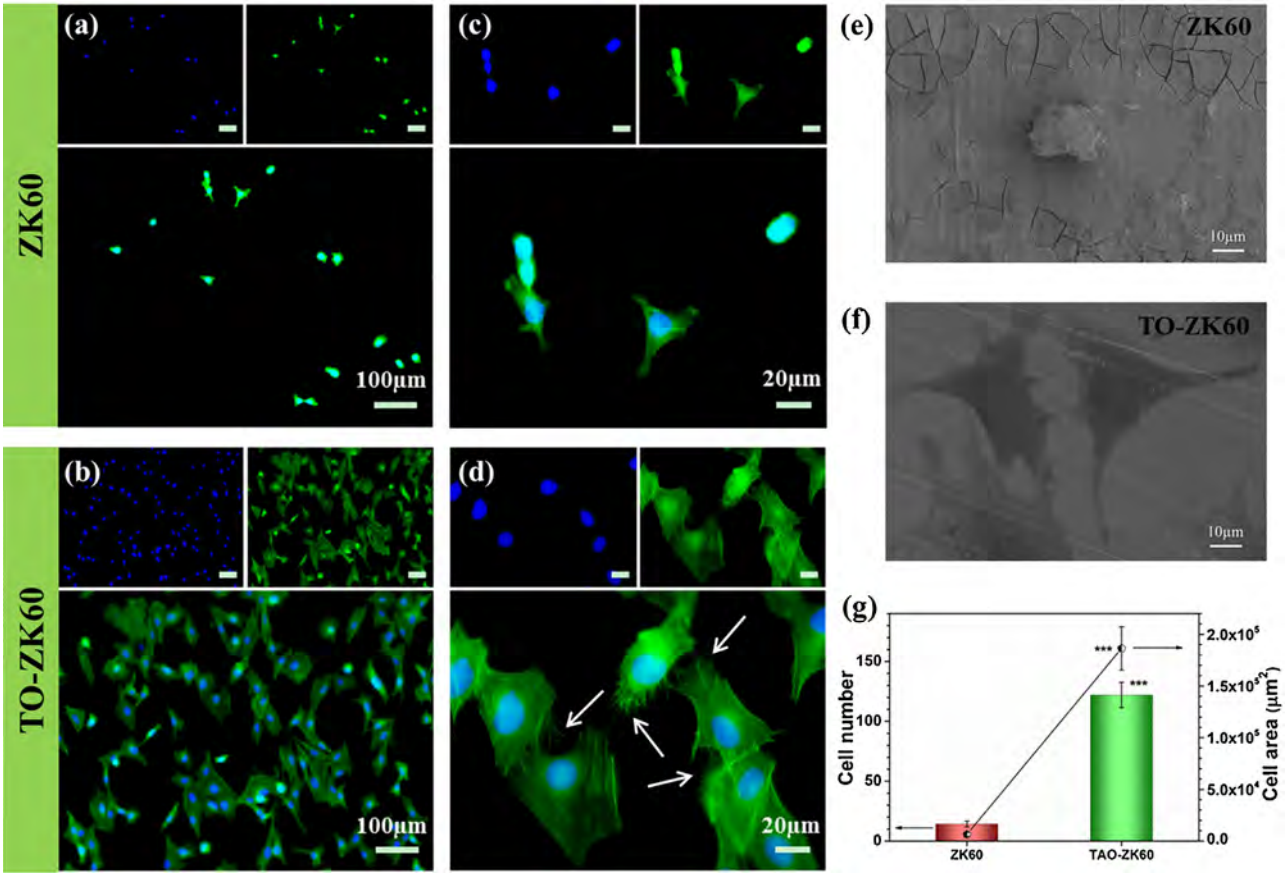

Fig. 7. Fluorescent images of the MC3T3-E1 pre-osteoblasts after incubation for 8 h on (a, c) ZK60 and (b, d) TO-ZK60. SEM images of the MC3T3-E1 pre-osteoblasts on (e) ZK60 and (f) TO-ZK60. (g) Cell number and cell area measured by counting the cell nuclei in (a) and (b). ***P < 0.001 compared to ZK60.

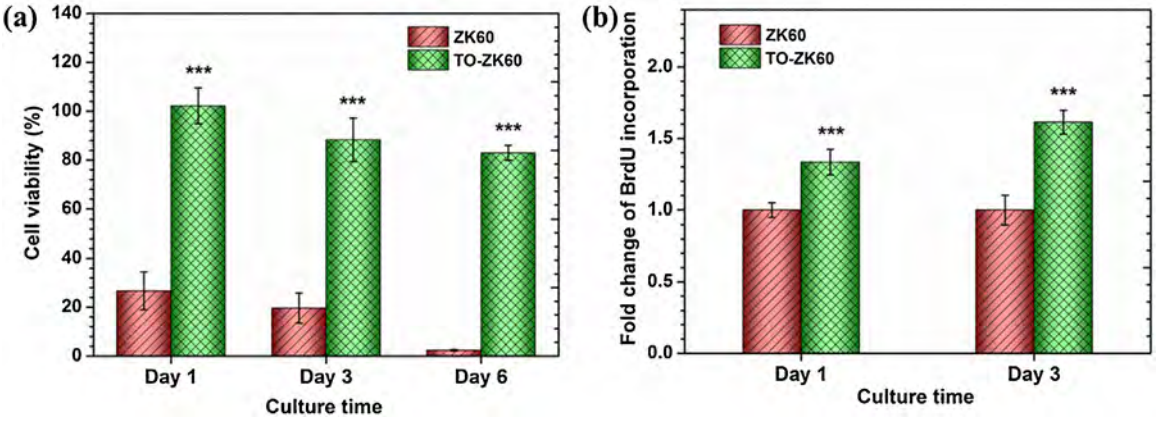

Fig. 8. (a) *in vitro* viability of the MC3T3-E1 pre-osteoblasts cultured with 70% extract of ZK60 and TO-ZK60 for 1, 3, and 6 days and (b) cell proliferation evaluated by the fold change of the incorporation of BrdU of 50% extract of ZK60 and TO-ZK60 for 1 and 3 days. ***P < 0.001 compared to ZK60.

possible corrosion products in the extracts may be filtered, the real conditions of the extracts prepared in the future will be maintained. The P and Ca concentrations in the TO-ZK60 extracts are very close to that in DMEM, suggesting that corrosion of ZK60 by the corrosive ions in DMEM is retarded to a great extent by the sputtered Ta-containing film.

The Mg ion concentration in the ZK60 extracts increases greatly to 559.7 ug/mL meaning more Mg ions are released from the untreated ZK60 during immersion in DMEM. In contrast, only a small concentration of Mg of 25.3 ug/mL is determined from the TO-ZK60 extracts. As the second most abundant cation in the human body, Mg is involved in energy metabolism and protein synthesis and plays an important physiological role particularly in the brain, heart, and skeletal muscles [64]. As shown by the previous studies, the MC3T3-E1 pre-osteoblast viability and differentiation after culturing in the medium containing 50 ug/mL Mg ions is significantly enhanced. However, exposure to large concentrations of Mg^{2+} especially over 200 ug/mL results in smaller viable rates of MC3T3-E1 cells [65]. As a result, the large amount of Mg^{2+} leached from the ZK60 Mg alloy imposes an adverse effect on cell growth and the Ta-containing film retards Mg dissolution and improves the situation.

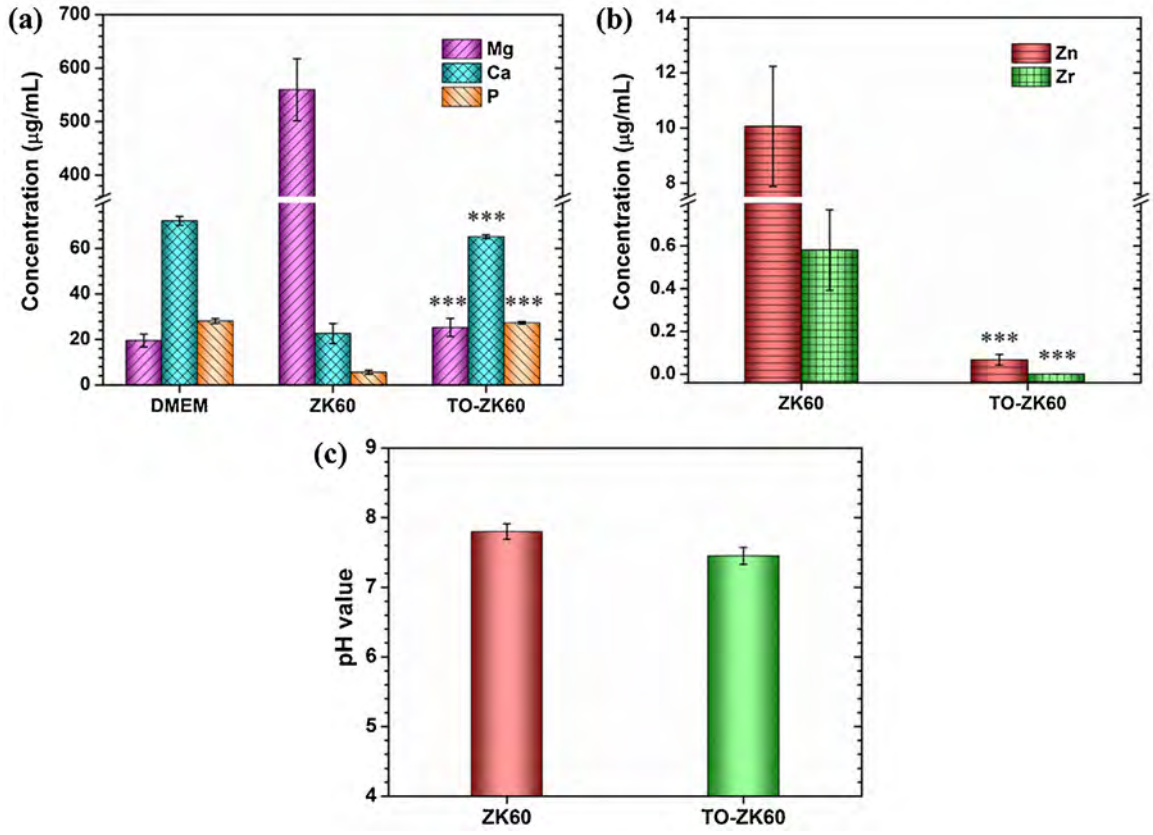

Fig. 9. Concentrations of (a) Mg, Ca, P and (b) Zn, and Zr in the extract of ZK60 and TO-ZK60; (c) Corresponding pH of the ZK60 and TO-ZK60 extract. ***P < 0.001 compared to ZK60.

The alloying elements in ZK60 including Zn and Zr in the extracts are monitored (Fig. 9(b)). The Zn concentration decreases from 10.06 ug/mL to 0.58 ug/mL after surface modification. Almost no Zr is detected from the TO-ZK60 extracts and a small concentration of 0.07 ug/mL of Zr is leached from the ZK60 Mg alloy. The local concentration of these elements may be larger than those in the collected extracts. As one of the vital elements in the human body, Zn plays important roles in the structure and function of many enzymes and other macromolecules. The cellular response to Zn^{2+} varies in a dose-dependent manner. Ma et al. evaluated the short-term cellular behavior of primary human coronary artery endothelial cells exposed to a concentration gradient of extracellular Zn^{2+} and found that small concentrations of Zn^{2+} (0–3.9 ug/mL) promoted cell adhesion, proliferation, and migration and enhanced expression of genes related to cell adhesion, cell injury, cell growth, angiogenesis, inflammation, vessel tone, and coagulation. However, large concentrations of Zn^{2+} (5.2–9.1 ug/mL) yielded opposite effects [66]. Another study reported that after pretreatment with 1 μg/mL Zn^{2+}, endothelial cells showed unhindered growth, significantly increased cellular vitality, and larger cellular proliferation rates. In contrast, 5 μg/mL of Zn^{2+} induced conflicting effects. After incubation with 10 μg/mL Zn^{2+}, the endothelial cells produced more cellular damage, cellular vitality, proliferation rates, as well as reduced enzyme activity [67]. The amount of Zn ions released from the untreated ZK60 Mg alloy is as large as 10.06 ug/mL, which is toxic to cells and inhibits normal cell behavior. Even though the extracts are diluted by 70% and 50% using the cell culture medium, the Zn^{2+} concentration is still quite large thus negatively affecting the cell behavior. In contrast, the concentration of Zn released from TO-ZK60 is only 0.58 ug/mL which is expected to produce positive effects on cell adhesion, spreading, growth, and proliferation. All in all, controlled release of Mg, Zn, and Zr is accomplished after the surface treatment of the ZK60 Mg alloy giving rise to the observed improved cytocompatibility *in vitro*.

As shown in Fig. 9(c), the corresponding pH value measured from the TO-ZK60 extracts is 7.45 ± 0.12 which is smaller than 7.80 ± 0.11 measured from the untreated ZK60 extracts. This slight increase in pH may not cause significant effects on indirect cell proliferation. Actually, the local pH at the corrosion region is probably larger and may have more pronounced effects on direct cell adhesion and spreading. This pH increase can be ascribed to the OH^- species formed during Mg corrosion and after surface modification; a more suitable pH is maintained for cell growth. In general, leached ions with high concentrations and subsequent increased pH caused by Mg degradation adversely influence *in vitro* cell attachment, spreading, growth, and proliferation and the sputtered Ta-containing film is effective in enhancing the cellular response. It should be noted that the extracts are filtered prior to the *in vitro* studies to avoid possible contamination in this work. Nonetheless, the degradability and biocompatibility of the detached particles from the alloy and deposited films caused by substrate corrosion and film breakage should be considered and further examined in future work in order to evaluate the long-term effects.

4. Conclusion

Ta-containing films are prepared on the ZK60 Mg alloy to retard corrosion and enhance the cytocompatiblity. The 4.8 μm thick stable and protective surface layer comprising Ta_2O_5, Ta suboxide, and Ta formed on the ZK60 Mg alloy yields I_{corr} of 1.334 ± 0.066 μA/cm^2 in SBF, which is 543 times smaller than that of the untreated substrate. The film resistance and transfer resistance of the TO-ZK60 sample in SBF increase from 59.46 Ω cm^2 (ZK60) to 2.313×10^4 Ω cm^2 and 12.57 Ω cm^2 (ZK60) to 2.870×10^4 Ω cm^2,

respectively. A loose and thicker corrosion product layer is formed on the untreated ZK60 Mg alloy after immersion in SBF for 3, 24, and 48 h, whereas only a few pits and shallow penetration of the aggressive medium into the substrate are observed from the TO-ZK60 sample even after immersion in SBF for 48 h. Our results show that the Ta-containing film improves both the corrosion resistance and biological properties of the ZK60 Mg alloy. The remarkable enhancement in the corrosion resistance is attributed to the stable and protective Ta_2O_5, Ta suboxides, and Ta surface. In addition, the Ta-containing layer provides a favorable surface for cell attachment, spreading, and proliferation as a result of the improved corrosion resistance, less leaching of Mg and alloying elements from the substrate, and more suitable pH. Our study suggests an effective strategy to improve the corrosion resistance and cytocompatibility of the ZK60 Mg alloy by surface functionalization with Ta.

Acknowledgments

This work is financially supported by City University of Hong Kong Research Grants Council (RGC) General Research Funds (GRF) CityU11301215 and Hong Kong Strategic Research Grant (SRG) No. 7004188.

References

[1] F. Witte, J. Fischer, J. Nellesen, H.A. Crostack, V. Kaese, A. Pisch, F. Beckmann, H. Windhagen, In vitro and in vivo corrosion measurements of magnesium alloys, Biomaterials 27 (2006) 1013–1018.
[2] F. Witte, V. Kaese, H. Haferkamp, E. Switzer, A. Meyer-Lindenberg, C.J. Wirth, H. Windhagen, In vivo corrosion of four magnesium alloys and the associated bone response, Biomaterials 26 (2005) 3557–3563.
[3] R. Erbel, C. Di Mario, J. Bartunek, J. Bonnier, B. de Bruyne, F.R. Eberli, P. Erne, M. Haude, B. Heublein, M. Horrigan, Temporary scaffolding of coronary arteries with bioabsorbable magnesium stents: a prospective non-randomised multicentre trial, Lancet 369 (2007) 1869–1875.
[4] R. Waksman, R. Pakala, P.K. Kuchulakanti, R. Baffour, D. Hellinga, R. Seabron, F.O. Tio, E. Wittchow, S. Hartwig, C. Harder, Safety and efficacy of bioabsorbable magnesium alloy stents in porcine coronary arteries, Catheter. Cardiovasc. Interv. 68 (2006) 607–617.
[5] F. Witte, N. Hort, C. Vogt, S. Cohen, K.U. Kainer, R. Willumeit, F. Feyerabend, Degradable biomaterials based on magnesium corrosion, Curr. Opin. Solid State Mater. Sci. 12 (2008) 63–72.
[6] G. Mani, M.D. Feldman, D. Patel, C.M. Agrawal, Coronary stents: a materials perspective, Biomaterials 28 (2007) 1689–1710.
[7] M.P. Staiger, A.M. Pietak, J. Huadmai, G. Dias, Magnesium and its alloys as orthopedic biomaterials: a review, Biomaterials 27 (2006) 1728–1734.
[8] G. Song, Control of biodegradation of biocompatable magnesium alloys, Corros. Sci. 49 (2007) 1696–1701.
[9] Y.F. Zheng, X.N. Gu, F. Witte, Biodegradable metals, Mater. Sci. Eng. R-Reports 77 (2014) 1–34.
[10] S. Virtanen, Biodegradable mg and Mg alloys: corrosion and biocompatibility, Mater. Sci. Eng.: B 176 (2011) 1600–1608.
[11] X. Gu, Y. Zheng, Y. Cheng, S. Zhong, T. Xi, In vitro corrosion and biocompatibility of binary magnesium alloys, Biomaterials 30 (2009) 484–498.
[12] Z. Li, X. Gu, S. Lou, Y. Zheng, The development of binary Mg-Ca alloys for use as biodegradable materials within bone, Biomaterials 29 (2008) 1329–1344.
[13] S. Zhang, X. Zhang, C. Zhao, J. Li, Y. Song, C. Xie, H. Tao, Y. Zhang, Y. He, Y. Jiang, Y. Bian, Research on an Mg-Zn alloy as a degradable biomaterial, Acta Biomater. 6 (2010) 626–640.
[14] J.E. Gray, B. Luan, Protective coatings on magnesium and its alloys – a critical review, J. Alloys Compd. 336 (2002) 88–113.
[15] H. Hornberger, S. Virtanen, A.R. Boccaccini, Biomedical coatings on magnesium alloys – A review, Acta Biomater. 8 (2012) 2442–2455.
[16] Y. Zhao, K.W.K. Yeung, P.K. Chu, Functionalization of biomedical materials using plasma and related technologies, Appl. Surf. Sci. 310 (2014) 11–18.
[17] G. Wu, J.M. Ibrahim, P.K. Chu, Surface design of biodegradable magnesium alloys—a review, Surf. Coat. Technol. 233 (2013) 2–12.
[18] L. Zhang, J.Q. Zhang, C.F. Chen, Y.H. Gu, Advances in microarc oxidation coated AZ31 Mg alloys for biomedical applications, Corros. Sci. 91 (2015) 7–28.
[19] I.M. Pohrelyuk, V.M. Fedirko, O.V. Tkachuk, R.V. Proskurnyak, Corrosion resistance of Ti-6Al-4 V alloy with nitride coatings in Ringer's solution, Corros. Sci. 66 (2013) 392–398.
[20] Y. Cheng, Y. Zheng, Characterization of TiN, TiC and TiCN coatings on Ti-50.6 at.% Ni alloy deposited by PIII and deposition technique, Surf. Coat. Technol. 201 (2007) 4909–4912.
[21] H.C. Barshilia, K. Rajam, Growth and characterization of chromium oxide coatings prepared by pulsed-direct current reactive unbalanced magnetron sputtering, Appl. Surf. Sci. 255 (2008) 2925–2931.
[22] H. Matsuno, A. Yokoyama, F. Watari, M. Uo, T. Kawasaki, Biocompatibility and osteogenesis of refractory metal implants titanium, hafnium, niobium, tantalum and rhenium, Biomaterials 22 (2001) 1253–1262.
[23] B.R. Levine, S. Sporer, R.A. Poggie, C.J. Della Valle, J.J. Jacobs, Experimental and clinical performance of porous tantalum in orthopedic surgery, Biomaterials 27 (2006) 4671–4681.
[24] W. Wilhelmsen, Passive behaviour of tantalum, Electrochim. Acta 33 (1988) 63–67.
[25] G. Palit, K. Elayaperumal, Passivity and pitting of corrosion resistant pure metals Ta, Nb Ti, Zr, Cr and A1 in chloride solutions, Corros. Sci. 18 (1978) 169–179.
[26] D.F. Taylor, Acid corrosion resistance of tantalum columbium, zirconium, and titanium, Ind. Eng. Chem. 42 (1950), 639–639.
[27] S. Maeng, L. Axe, T.A. Tyson, L. Gladczuk, M. Sosnowski, Corrosion behaviour of magnetron sputtered alpha- and beta-Ta coatings on AISI 4340 steel as a function of coating thickness, Corros. Sci. 48 (2006) 2154–2171.
[28] S.Z. El Abedin, U. Welz-Biermann, F. Endres, A study on the electrodeposition of tantalum on NiTi alloy in an ionic liquid and corrosion behaviour of the coated alloy, Electrochem. Commun. 7 (2005) 941–946.
[29] B. Diaz, J. Swiatowska, V. Maurice, A. Seyeux, E. Harkonen, M. Ritala, S. Tervakangas, J. Kolehmainen, P. Marcus, Tantalum oxide nanocoatings prepared by atomic layer and filtered cathodic arc deposition for corrosion protection of steel: comparative surface and electrochemical analysis, Electrochim. Acta 90 (2013) 232–245.
[30] P.M. Natishan, E. McCafferty, P.R. Puckett, S. Michel, Ion beam assisted deposited tantalum oxide coatings on aluminum, Corros. Sci. 38 (1996) 1043–1049.
[31] B. Diaz, J. Swiatowska, V. Maurice, M. Pisarek, A. Seyeux, S. Zanna, S. Tervakangas, J. Kolehmainen, P. Marcus, Chromium and tantalum oxide nanocoatings prepared by filtered cathodic arc deposition for corrosion protection of carbon steel, Surf. Coat. Technol. 206 (2012) 3903–3910.
[32] T. Lu, J. Wen, S. Qian, H. Cao, C. Ning, X. Pan, X. Jiang, X. Liu, P.K. Chu, Enhanced osteointegration on tantalum-implanted polyetheretherketone surface with bone-like elastic modulus, Biomaterials 51 (2015) 173–183.
[33] J. Liu, X. Xu, P. Lu, Electrochemical corrosion behavior of nanocrystalline β-Ta coating for biomedical applications, ACS Biomater. Sci. Eng. 2 (2016) 579–594.
[34] Y.-S. Sun, J.-H. Chang, H.-H. Huang, Corrosion resistance and biocompatibility of titanium surface coated with amorphous tantalum pentoxide, Thin Solid Films 528 (2013) 130–135.
[35] G. Xu, X. Shen, Y. Hu, P. Ma, K. Cai, Fabrication of tantalum oxide layers onto titanium substrates for improved corrosion resistance and cytocompatibility, Surf. Coat. Technol. 272 (2015) 58–65.
[36] K. McNamara, O. Kolaj-Robin, S. Belochapkine, F. Laffir, A.A. Gandhi, S.A.M. Tofail, Surface chemistry and cytotoxicity of reactively sputtered tantalum oxide films on NiTi plates, Thin Solid Films 589 (2015) 1–7.
[37] H.-L. Huang, Y.-Y. Chang, H.-J. Chen, Y.-K. Chou, C.-H. Lai, M.Y. Chen, Antibacterial properties and cytocompatibility of tantalum oxide coatings with different silver content, J. Vac. Sci. Technol. A 32 (2014) 02B117.
[38] T. Kokubo, H. Takadama, How useful is SBF in predicting in vivo bone bioactivity? Biomaterials 27 (2006) 2907–2915.
[39] J. Moulder, W. Stickle, P. Sobol, K. Bomben, in: J. Chastain (Ed.), Handbook of X-Ray Photoelectron Spectroscopy, Perkin-Elmer Corporation, Physical Electronics Division, 1992.
[40] J.Y. Zhang, I.W. Boyd, Thin tantalum and tantalum oxide films grown by pulsed laser deposition, Appl. Surf. Sci. 168 (2000) 234–238.
[41] Y. Cheng, W. Cai, Y.F. Zheng, H.T. Li, L.C. Zhao, Surface characterization and immersion tests of TiNi alloy coated with Ta, Surf. Coat. Technol. 190 (2005) 428–433.
[42] R. Lahoz, J. Pedro Espinos, F. Yubero, A. Rodriguez Gonzalez-Elipe, G. Francisco de la Fuente, In situ XPS studies of laser-induced surface nitridation and oxidation of tantalum, J. Mater. Res. 30 (2015) 2967–2976.
[43] Y. Cheng, W. Cai, H.T. Li, Y.F. Zheng, L.C. Zhao, Surface characteristics and corrosion resistance properties of TiNi shape memory alloy coated with Ta, Surf. Coat. Technol. 186 (2004) 346–352.
[44] M. Zhu, Z. Zhang, W. Miao, Intense photoluminescence from amorphous tantalum oxide films, Appl. Phys. Lett. 89 (2006).
[45] H. Li, Y. Muraki, K. Karahashi, S. Hamaguchi, Suboxide/subnitride formation on Ta masks during magnetic material etching by reactive plasmas, J. Vac. Sci. Technol. A 33 (2015).
[46] W. Kulisch, D. Gilliland, G. Ceccone, L. Sirghi, H. Rauscher, P.N. Gibson, M. Zuern, F. Bretagnol, F. Rossi, Ion beam sputtering of Ta(2)O(5) films on thermoplast substrates as waveguides for biosensors, J. Vac. Sci. Technol. B 27 (2009) 1180–1190.
[47] Y.-Y. Chang, H.-L. Huang, H.-J. Chen, C.-H. Lai, C.-Y. Wen, Antibacterial properties and cytocompatibility of tantalum oxide coatings, Surf. Coat. Technol. 259 (2014) 193–198.
[48] X. He, J. Wu, X. Li, X. Gao, L. Wu, L. Zhao, X. Gan, F. Zhuge, Characterization of high quality tantalum pentoxide film synthesized by oxygen plasma enhanced pulsed laser deposition, Thin Solid Films 518 (2009) 94–98.
[49] E. McCafferty, Validation of corrosion rates measured by the Tafel extrapolation method, Corros. Sci. 47 (2005) 3202–3215.

[50] M.I. Jamesh, G. Wu, Y. Zhao, D.R. McKenzie, M.M.M. Bilek, P.K. Chu, Effects of zirconium and oxygen plasma ion implantation on the corrosion behavior of ZK60 Mg alloy in simulated body fluids, Corros. Sci. 82 (2014) 7–26.
[51] R. Xu, X. Yang, P. Li, K.W. Suen, S. Wu, P.K. Chu, Eelectrochemical properties and corrosion resistance of carbon-ion-implanted magnesium, Corros. Sci. 82 (2014) 173–179.
[52] X. Li, Z. Weng, W. Yuan, X. Luo, H.M. Wong, X. Liu, S. Wu, K.W.K. Yeung, Y. Zheng, P.K. Chu, Corrosion resistance of dicalcium phosphate dihydrate/poly(lactic-co-glycolic acid) hybrid coating on AZ31 magnesium alloy, Corros. Sci. 102 (2016) 209–221.
[53] W. Zhou, T. Shen, N.N. Aung, Effect of heat treatment on corrosion behaviour of magnesium alloy AZ91D in simulated body fluid, Corros. Sci. 52 (2010) 1035–1041.
[54] G.-L. Song, Z. Shi, Corrosion mechanism and evaluation of anodized magnesium alloys, Corros. Sci. 85 (2014) 126–140.
[55] Y. Zhao, M.I. Jamesh, W.K. Li, G. Wu, C. Wang, Y. Zheng, K.W.K. Yeung, P.K. Chu, Enhanced antimicrobial properties, cytocompatibility, and corrosion resistance of plasma-modified biodegradable magnesium alloys, Acta Biomater. 10 (2014) 544–556.
[56] J. Zhang, C. Dai, J. Wei, Z. Wen, S. Zhang, C. Chen, Degradable behavior and bioactivity of micro-arc oxidized AZ91D Mg alloy with calcium phosphate/chitosan composite coating in m-SBF, Colloids Surf. B-Biointerfaces 111 (2013) 179–187.
[57] M.I. Jamesh, G. Wu, Y. Zhao, W. Jin, D.R. McKenzie, M.M.M. Bilek, P.K. Chu, Effects of zirconium and nitrogen plasma immersion ion implantation on the electrochemical corrosion behavior of Mg-Y-RE alloy in simulated body fluid and cell culture medium, Corros. Sci. 86 (2014) 239–251.
[58] Y. Chen, X. Wang, J. Li, J. Lu, F. Wang, Long-term anticorrosion behaviour of polyaniline on mild steel, Corros. Sci. 49 (2007) 3052–3063.
[59] C. Liu, Q. Bi, A. Leyland, A. Matthews, An electrochemical impedance spectroscopy study of the corrosion behaviour of PVD coated steels in 0.5 N NaCl aqueous solution: part II.: EIS interpretation of corrosion behaviour, Corros. Sci. 45 (2003) 1257–1273.
[60] X. Zhang, X.-W. Li, J.-G. Li, X.-D. Sun, Preparation and characterizations of bioglass ceramic cement/Ca-P coating on pure magnesium for biomedical applications, ACS Appl. Mater. Inter. 6 (2014) 513–525.
[61] M.I. Jamesh, G. Wu, Y. Zhao, D.R. McKenzie, M.M.M. Bilek, P.K. Chu, Electrochemical corrosion behavior of biodegradable Mg-Y-RE and Mg-Zn-Zr alloys in Ringer's solution and simulated body fluid, Corros. Sci. 91 (2015) 160–184.
[62] W. Jin, G. Wu, H. Feng, W. Wang, X. Zhang, P.K. Chu, Improvement of corrosion resistance and biocompatibility of rare-earth WE43 magnesium alloy by neodymium self-ion implantation, Corros. Sci. 94 (2015) 142–155.
[63] Y. Zhao, G. Wu, Q. Lu, J. Wu, R. Xu, K.W.K. Yeung, P.K. Chu, Improved surface corrosion resistance of WE43 magnesium alloy by dual titanium and oxygen ion implantation, Thin Solid Films 529 (2013) 407–411.
[64] R.E. Wildman, D.M. Medeiros, Advanced Human Nutrition, CRC Press, 1999.
[65] H.M. Wong, S. Wu, P.K. Chu, S.H. Cheng, K.D.K. Luk, K.M.C. Cheung, K.W.K. Yeung, Low-modulus Mg/PCL hybrid bone substitute for osteoporotic fracture fixation, Biomaterials 34 (2013) 7016–7032.
[66] J. Ma, N. Zhao, D. Zhu, Endothelial cellular responses to biodegradable metal zinc, ACS Biomater. Sci. Eng. 1 (2015) 1174–1182.
[67] A. Szuster-Ciesielska, A. Stachura, M. Slotwinska, T. Kaminska, R. Sniezko, R. Paduch, D. Abramczyk, J. Filar, M. Kandefer-Szerszen, The inhibitory effect of zinc on cadmium-induced cell apoptosis and reactive oxygen species (ROS) production in cell cultures, Toxicology 145 (2000) 159–171.